A Method to Achieve High Dynamic Range in a CMOS Image Sensor Using Interleaved Row Readout

Thomas Wocial, Konstantin D. Stefanov, *Member, IEEE*, William E. Martin, John R. Barnes, and Hugh R. A. Jones

***Abstract*—We present a readout scheme for CMOS image sensors that can be used to achieve arbitrarily high dynamic range (HDR) in principle. The linear full well capacity (LFWC) in high signal regions was extended 50 times from 20 to 984 ke$^-$ via an interlaced row-wise readout order, while the noise floor remained unchanged in low signal regions, resulting in a 34-dB increase in DR. The peak signal-to-noise ratio (PSNR) is increased in a continuous fashion from 43 to 60 dB. This was achieved by summing user-selected rows that were read out multiple times. Centroiding uncertainties were lowered when template-fitting a projected pattern, compared to the standard readout scheme. Example applications are aimed at scientific imaging due to the linearity and PSNR increase.**

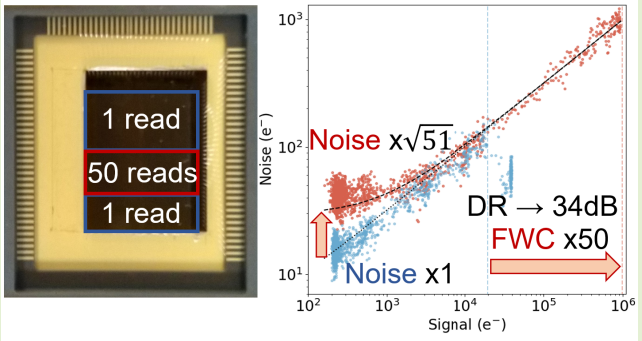

***Index Terms*—CMOS, dynamic range (DR), image sensor, local integration time, random addressing, row-wise.**

I. Introduction

IN RECENT years, the CMOS image sensor (CIS) has seen increased adoption by the astronomical community, particularly in time-domain applications [1]. First invented in 1993 [2], some advantages of the active pixel architecture over charge-coupled devices (CCDs) include: 1) ability for faster readout; 2) readout from region of interest (ROI); 3) low power; 4) low readout noise; and 5) built-in antiblooming.

A variety of techniques exist to extend the dynamic range (DR) of CISs. These have previously been classified into seven categories: 1) logarithmic pixel response; 2) combined linear and logarithmic response; 3) well capacity adjustment; 4) frequency-based sensors; 5) time-to-saturation-based sensors; 6) global control of integration; and 7) local control over integration [3], [4]. Other advances that result in an increased DR include improved dark current suppression, lower read noise, and multigain readout [5].

The 4/5T pixel architecture is widely employed in scientific imaging, but the selection of DR extension techniques is limited. For instance, DRs of 160 dB have been achieved in CIS using a 3T architecture with integrated charge compensation photodiode [6] and 141 dB (proposed) on 4T architecture with a lateral overflow integration capacitor but both suffer from nonlinear pixel responses and signal-to-noise ratio (SNR) curves. DR extension techniques used for comparison to this work will apply to 4T pixels and therefore fall under local control over integration and global control over integration.

For the scientific requirement and operation of our CIS, key assumptions are made about the scene to be imaged: 1) there exists a desired minimum SNR of the observation and, hence, minimum integration time; 2) the scene is spatially and temporally static; and 3) it is always desirable to achieve the maximum possible SNR for any local region.

Self-reset pixels achieve high DR (HDR) by locally controlling integration time. The pixel is based on the 4T architecture with additional circuitry to trigger a reset signal when the voltage at the sense node matches a reference corresponding to the full well capacity (FWC). By counting the triggers and sampling the residual voltage, it is possible to reconstruct

Manuscript received 13 August 2022; revised 11 September 2022; accepted 14 September 2022. Date of publication 6 October 2022; date of current version 14 November 2022. The work of Thomas Wocial, William E. Martin, and Hugh R. A. Jones was supported by the Science and Technology Facilities Council (STFC) under Grant ST/W507490/1, Grant ST/W508020/1, Grant ST/P005667/1, and Grant ST/R006598/1. The work of Konstantin D. Stefanov and John R. Barnes was supported by Open University through the Research, Enterprise and Scholarship Innovation Grant. The associate editor coordinating the review of this article and approving it for publication was Prof. Kazuaki Sawada. *(Corresponding author: Thomas Wocial.)*

Thomas Wocial, William E. Martin, and Hugh R. A. Jones are with the Centre for Astrophysics Research, University of Hertfordshire, AL10 9AB Hatfield, U.K. (e-mail: t.wocial@herts.ac.uk).

Konstantin D. Stefanov and John R. Barnes are with the School of Physical Sciences, Open University, MK7 6AA Milton Keynes, U.K. (e-mail: konstantin.stefanov@open.ac.uk).

Digital Object Identifier 10.1109/JSEN.2022.3211152

photosignals that would otherwise exceed the pixel FWC for a given integration while preserving linearity. Recent implementations include a 16 × 16 pixel on 20-μm pitch at 121-dB DR [7] and 96 × 128 pixels on 25-μm pitch at 125-dB DR [8]. Fill factors are 13.1% and 10%. A key advantage is the continuous SNR increase with photosignal, and however, the low fill factor, large pitch, and small array sizes can be a challenge for use in scientific imaging.

Multiple exposure is a commonly employed technique to increase DR without the need for additional circuitry. Dual exposure involves acquiring two images at different integration times T_{long} and T_{short} with the DR extension equal to $T_{\text{long}}/T_{\text{short}}$ [9], [10]. There exists an SNR dip in regions corresponding to saturation in the short exposure, as the photosignal here is only sampled for a fraction of the total integration time. The use of multiple shorter integrations can lower the resulting SNR dip [11].

Nondestructive readout (NDR) operates by sampling the signal many times during the integration time without affecting the built-up photocharge. The CIS is read with up-the-ramp sampling, as widely used on IR photodiode arrays for DR increase [12], [13] and for cosmic ray rejection [14].

Coded rolling shutter [15] works by spatially varying exposure per row, achieving a DR increase up to the ratio of longest and shortest exposure times. Image reconstruction is needed as vertical spatial information may be lost, and however, due to the encoded temporal information, high-speed video and optical flow can be extracted [16], [17]. Interleaved multiple gain readout has been used to achieve a DR of 120 dB [18]. Work in this area is limited by commercial CIS devices often being addressable row-wise only, pixel-wise coded exposure could be achieved with full X–Y addressability [16].

Pixel-wise control of integration times builds on row-wise coded exposure by the addition of control over an additional spatial dimension. Recent advances in 3-D stacked CIS devices have not enabled a pixel-parallel architecture, typically based on Cu–Cu interconnects between the sensing and logic layers [19]. A similar method is to control the exposure for a block of pixels, as shown in [20] and [21]. In [22], a 512 × 512 array with 4.6-μm pitch on a 3-D integrated circuit (IC) achieves 127-dB DR by combining dual conversion gain with time-to-saturation detection. Key advantages are the high spatial fidelity achieved with a pixel-parallel readout, and however, there is noncontinuity in the SNR response due to the three photosensing regimes.

In this article, a row-wise coded exposure scheme is proposed, which varies exposure locally depending on the illumination, with multiple subexposures occurring in said regions to exceed the SNR limit imposed by the FWC of the pixel. A hardware demonstration on a Teledyne e2v (Te2v) SIRIUS CIS115 [23] results in extended DR and peak SNR (PSNR). This is achieved due to the ability to randomly address and read out rows. A future implementation of this technique is for actively controlled spectroscopy [24], as both high signal calibration spectral lines and science spectral lines fall on the focal plane [25], [26]. Other applications may include multi-ROI imaging at varying subexposures and other areas, where HDR and SNR images are of interest. The ability for CISs to operate in such a way has been recognized by others [27], [28] but to our knowledge has not been implemented in scientific imaging applications.

TABLE I
SPECIFICATIONS FOR CIS115 [23]

	Unit	CIS115
Active rows		2000
Active columns		1504
Pixel size	μm	7.0
Non-linearity	±%	3
Mean read noise	e^-	5
Peak linear charge	e^-/pix	27,000
Saturation charge	e^-/pix	33,000
Dynamic range	dB	74.6
Dark current	e^-/pix/s	20 (at 293 K)
DSNU	e^-/pix/s	12 (at 293 K)

II. Dynamic Range

A scene's DR is given by the upper and lower limits of its luminance range. It is desirable for a CIS to have an HDR as this means that it can faithfully quantify both the high and low signal regions in the scene. For a sensor with a linear FWC (LFWC) of Q_{well} (e^-), exposure time t (s), average dark current I_{dc} (e^-/s), and read noise variance σ^2_{read} (e^2), the DR is the ratio of maximum (I_{max}) and minimum (I_{min}) detectable photocurrents as in (1). The maximum detectable signal is limited by Q_{well} minus the dark signal (which is subtracted from a reference image taken in darkness), while the noise floor (assuming correlated double sampling (CDS) and fixed pattern noise correction) is determined by the read noise and dark current signal noise

$$\text{DR} = 20\ \log_{10}\frac{I_{\text{max}}}{I_{\text{min}}} = 20\ \log_{10}\frac{Q_{\text{well}} - I_{\text{dc}}t}{\sqrt{\sigma^2_{\text{read}} + I_{\text{dc}}t}}. \quad (1)$$

The readout noise determines the noise floor of a CIS. This value is almost independent of temperature and integration time. It is comprised of transistor noise from the source follower, amplifier, and analog-to-digital converter (ADC) noise. Quantization noise can contribute to read noise if the signal is sampled with low resolution. To determine the readout noise, we calculate the standard deviation of each pixel using a set of bias frames [29]. The input-referred noise is often given in equivalent noise charge, expressed in e^- rms.

Dark current occurs as a result of thermal excitation of electron–hole pairs in silicon. The sensor used in this article, CIS115, has a dark current of 20 e^-/pix/s at 293 K, which halves for every temperature reduction of 5.5 K [23]. If the noise floor is dominated by dark current, using shorter exposures or cooling the CIS can increase the DR.

III. Method

A. CIS115

The sensor used is a CIS115 from Te2v, featuring an array of 2000 × 1504 pixels on 7-μm pitch [23] (see Table I for measured BSI variant specifications). It employs the 4T pixel architecture and is fabricated using a 0.18-μm CIS process. The model used in this article is a front-side illuminated variant. A back-side illuminated variant has been adopted for

the JANUS instrument on JUICE [30], [31]. The sensor is divided into four blocks of 376 columns that are read out simultaneously and in parallel. Each pixel transfers the reset and signal levels to a storage buffer that allows for CDS to be performed. CIS115 operates in rolling shutter mode meaning that integration time is simultaneous for all pixels in a row. All control signals are generated externally.

B. Row-Wise HDR Readout Scheme

The scheme demonstrated in this article seeks to address the key traits for scientific imaging: pixel linearity and continuous SNR increase with photosignal. For a maximum per pixel photocurrent per row $I(M)$, a total integration time t, with row-wise control over exposure, the scheme is given as follows. If the FWC is reached or exceeded in t, perform N subexposures with a read and reset sample such that (2) is satisfied. N rows are summed (stacked) in software

$$N = \lceil I(M) \times t/\text{FWC} \rceil. \tag{2}$$

By doing so, the noise floor is kept at a minimum on a per-row basis and the PSNR is increased by sampling the maximum detectable photosignal multiple times. We implement a simplified version of this scheme with one region that can reconstruct photosignals 50 times greater than the FWC per integration.

CIS115 is mounted on a control PCB, with sensor interfacing achieved via a National Instruments PXIe-7856R FPGA card. A custom LabVIEW GUI was developed at Open University. In the standard configuration, the minimum row readout time, T_{row}, is 412.5 μs, so the readout time for the whole array once is 825 ms. During readout, the analog sensor outputs are digitized by four 16-bit ADCs in the PXIe-7856R card with the digital values stored as signed 32-bit integers. In this demonstration, HDR is achieved by sorting the rows (M_{Total}) into two groups: rows read out once (M_{Once}) and rows read out N additional times per integration (M_{HDR}). Integration time for rows read once T_{Once} [see (3)] is therefore N times larger than those read multiple times T_{HDR} [see (4)]. The signals from rows read multiple times are then summed to achieve the same total integration time with increased equivalent FWC

$$T_{\text{Once}} = T_{\text{row}} \times (M_{\text{Total}} + N \times M_{\text{HDR}}) \tag{3}$$

$$T_{\text{HDR}} = T_{\text{row}} \times (M_{\text{Total}}/N + M_{\text{HDR}}). \tag{4}$$

Rows read out multiple times have to be interleaved with rows read once to keep constant timing, as shown in a simplified timing diagram in Fig. 1. Here, the read noise in row three increases by a factor of $\sqrt{5+1}$ and effective FWC by a factor of 5. A readout is always accompanied by a photodiode reset. Each block is the sum of the CDS time (10 μs) and the row readout time for a total of 412.5 μs (not to scale). A delay timer can also be added, where no readout occurs. The total number of row readouts is $M_{\text{Total}} + N \times M_{\text{HDR}}$. The order in which rows are read is determined by M_{total} and N. In the HDR readout configuration used, these are 2000 and 50. If M_{total} does not divide by N to give an integer, then rows in M_{HDR} will not have constant timing due to rounding to the nearest row. The 40 rows used for HDR, M_{HDR}, are from

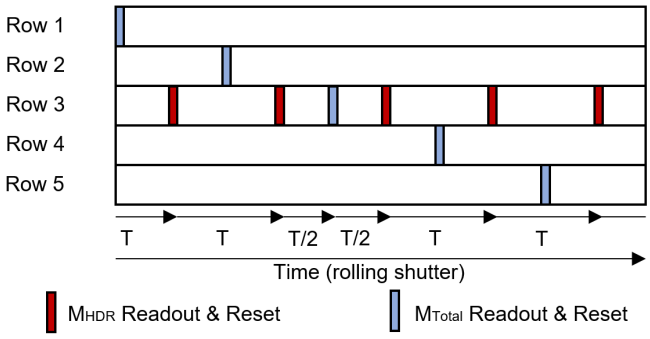

Fig. 1. Simplified row-wise timing diagram in rolling shutter operation. In this example, for $N = 5$, row 3 is read out six times in one integration, while the other four rows are just once. Integration occurs in the white regions with readout and reset samples in blue for the standard readout and in red for the HDR readout.

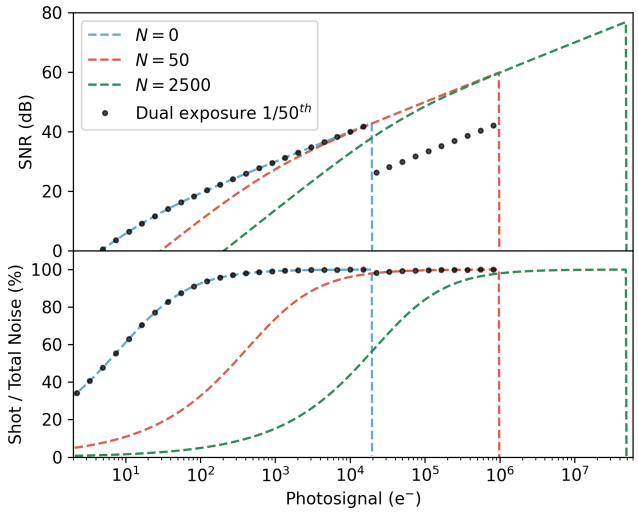

Fig. 2. Noise performance at varying photosignals for the HDR extension scheme described in this article. N is the number of additional row signal and reset samples per integration.

rows 1495 to 1534 in order to image the brightest centroid at row 1512. Each additional row read and reset sample increases the integration time by 412.5 μs. As 4000 row read and reset samples occur, the integration time is 1650 ms. This constrains use cases toward lower peak luminance HDR scenes, though a CIS with a shorter sample time would overcome this.

The last point is demonstrated with simulated performance in Fig. 2. The term N represents the number of additional row reads (hence stacked additional subframes) in a given region. With appropriate selection of row readouts and resets summed in a given integration period, the PSNR and maximum DR can be increased arbitrarily high with the photosignal (as in $N = 2500$) while simultaneously retaining improved noise characteristics in low signal regions ($N = 0$). The noise model is simplified, comprising read and shot noise only. Read noise and LFWC are the values found for our device at 4.1 e^- and 19.7 ke^-, respectively. For comparison, a dual exposure scheme with a 1:50 exposure ratio is shown by black markers. NDR and single read row-wise coded exposure exhibit equivalent SNR profiles. DR is extended by 34 dB as

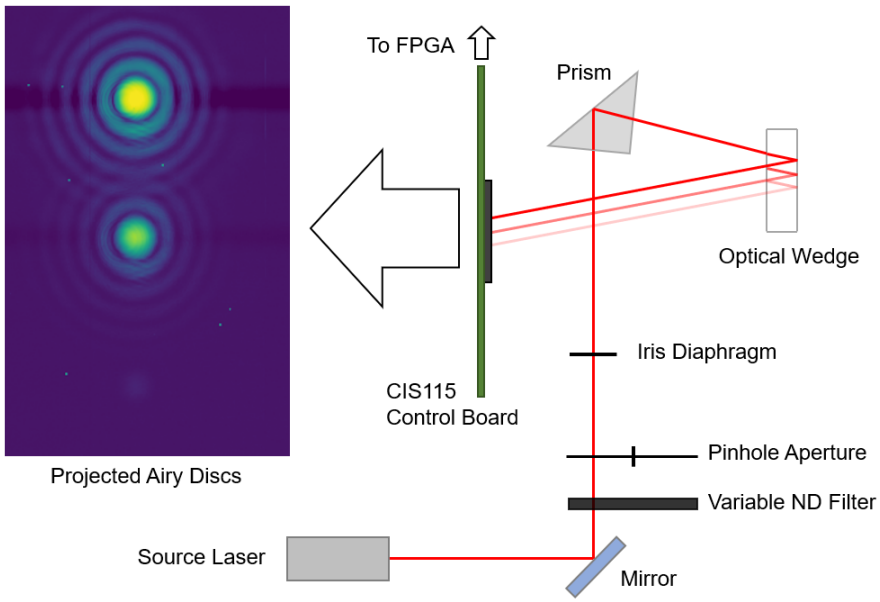

Fig. 3. Optical setup used. Laser source is a Thorlabs CPS532-C2, ND filter a Thorlabs NDC-50C-4, mirror, Thorlabs PHWM16 pinhole, 45° prism, a Thorlabs WW41050-A optical wedge, and the CIS115 board. The optics is used to project the three Airy disks shown in the top left.

with our method for N = 50, although there is a significant drop in SNR from 42.9 to 25.8 dB when the photosignal exceeds the FWC, with the PSNR remaining unchanged. In our method, SNR drops by only 0.2 dB and continues to rise to 59.9 dB over the same region.

Once the integration is complete, the image is saved as a 32-bit binary file with original sensor dimensions. When read with this HDR scheme, the effective FWC is increased by a factor of N and read noise increased by $\sqrt{N+1}$ for rows in M_{HDR}, with M_{Once} retaining original FWC and read noise. DR for the whole array is extended by a factor of $20\log_{10}(N)$ dB.

As a result, the DR of an imaged object is dependent on the sensor rows on which it appears. In this work, the limited readout bandwidth resulted in long integration times, so dark current noise contributions were comparable to read noise. This would ideally be reduced with higher readout rates. Timer control or reading dummy rows allow for more flexible readout orders. In addition, only two regions are used in this article, though schemes may have regions with multiple varying cadences.

C. Optics

A DR measurement can be performed using a flat field with either variable source intensity or integration time. This is achieved by measuring the linear FWC and read noise. This method is simple to perform and, however, does not allow for simultaneous noise analysis in low signal regions. By projecting an HDR pattern onto the CIS, a signal analysis can be performed for a continuous range of intensities allowing for quantification of artifacts introduced by the HDR extension technique.

An analysis is performed using the three reflected Airy disk patterns projected onto the focal plane (Fig. 3). First, a collimated 532-nm, 0.9-mW laser (Thorlabs CPS532-C2) is attenuated using an adjustable neutral density filter. A 300-μm pinhole aperture (Thorlabs PHWM16) produces the Airy disk with an adjustable iris used to spatially filter the beam to mitigate unwanted reflections. The beam profile is then picked off by a right-angled prism, to an optical wedge opposite to CIS115, at an angle of 30° (Thorlabs WW41050-A). Fine adjustment of the angles of the prism and wedge allows for spatial position of the pattern. The wedge can also be rotated. In this case, the wedge is rotated such that the three reflections lay on an axis parallel to the columns of CIS115, as shown in Fig. 3. The spatial filter was adjusted to block maxima greater than four. This helps mitigate against specular reflection from flat surfaces propagating through the optical path and stops the outer orders from the first Airy pattern swamping the signal from the second and third patterns. The laser was kept on for at least 10 min before taking measurements to mitigate heating effects

$$I(r_p) = I_0\left(\frac{2J_1(r_p ka\mu/h)}{r_p ka\mu/h}\right)^2. \tag{5}$$

In pixel units, the radial variation of intensity from the centroid on the image plane is given by (5), where r_p is the distance to the centroid in pixels, I_0 is the intensity normalization constant to be found, J_1 is the first-order Bessel function of the first kind, k is the wavenumber, a is the pinhole radius (150 μm), μ is the pixel size (7.0 μm), and h is the path length from pinhole to image plane. The small angle approximation is employed to convert to pixel units. Using a standard readout scheme and ensuring the Airy disk remained in the linear region, a line profile was taken and used to fit the Airy profile above. The value of $ka\mu/h$ was found to be equal to $3.89 \pm 0.01 \times 10^{-2}$ pix^{-1}. As other constants are known, h solves to be 318 ± 1 mm, exceeding the criterion

for far-field diffraction of D^2/λ. Setting the LHS of (5) as $I_0/2$ and solving for r_p gives a full-width and half-maximum (FWHM) of 83.1 ± 0.2 pixels, as shown in Fig. 8.

D. Artifacts

Image corrections are performed. The top left of Fig. 3 is an 825-ms integration with the three Airy disks visible. An 825-ms dark integration has been subtracted for correction of DSNU and FPN. Ten hot pixels are also visible in this image. Correction is applied using a bilinear interpolation. Four bad columns are replaced using linear interpolation. The final feature is a signal-dependent baseline shift from the expected value, that is, rows that fall on high signal regions deviate below the baseline value in low signal regions. This feature is visible in Fig. 3 (top left) as the darker blue horizontal bands that occur either side of the maxima of the first and second Airy disk. This is due to an offset of the ground return to the source follower column bias. This feature has been reduced significantly in some applications by creating dark reference pixels for correction.

It was found that the baseline deviation was proportional to the sum of all pixel values in a row. With CIS115 operating in HDR mode and the three Airy disks projected onto the focal plane, the median background level for a row is plotted against the sum of all pixels in the row (Σ_{Row}) in Fig. 3. Using a least-squares linear fit, the expected row-wide deviation is equal to -1.339×10^{-5} ADC unit (ADU) per Σ_{Row}. The light frames are then corrected using this relationship by multiplying with the row sum and adding to each pixel before linearity correction and conversion from ADU to e^-.

E. Sensor Characterization

1) System Gain: The system gain is defined as the number of photoelectrons generating an output signal of 1 ADU. It is comprised of the charge-to-voltage factor at the sense node, external amplification, and ADC voltage resolution. Gain can be calculated by measuring X-ray events from a radioactive ^{55}Fe source [31]. The decay to ^{55}Mn produces X-ray photons at 5898 and 6490 eV, depositing 1616 and 1778 photoelectrons in Si, respectively. Peaks visible at 1060 and 1165 ADU correspond to a system gain of 1.55 e^-/ADU.

2) Read Noise: It has been calculated using dark image subtraction to remove dc offsets. Due to the significant contribution from dark current associated with whole array readouts (825 ms), a 50 row $\times$ 376 column ROI is used due to the short readout time of 20 ms. Two images taken in darkness were subtracted and the standard deviation of the difference was divided by $\sqrt{2}$ giving a read noise of 4.1 e^-, agreeing with other reported values for CIS115 [31].

3) Linearity: The photoresponse of CIS115 was measured by varying the illumination time from a red LED in increments of 500 ms. A window of 200 $\times$ 200 pixels was selected when calculating the mean to avoid vignetting. In Fig. 4, the measured signal is shown until the deviation from a linear fit reaches 5%. This occurs at 4000 ms, corresponding to a signal of 11 235 ADU. The residuals form a polynomial with negative second derivative, due to nonlinearity brought on by increasing

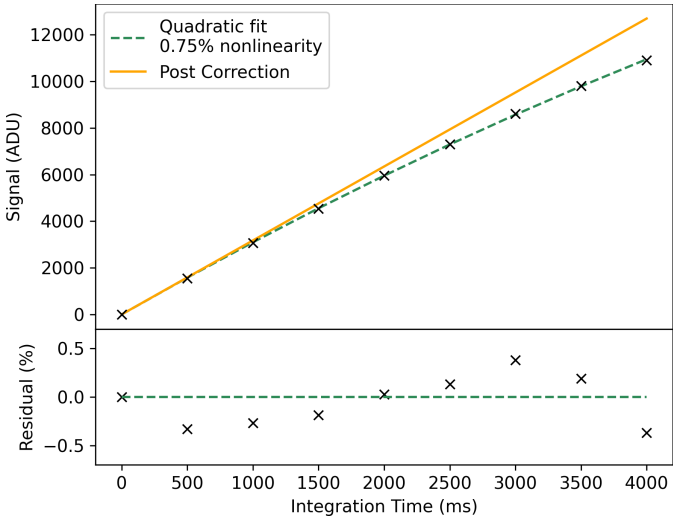

Fig. 4. Mean signal of a 200 $\times$ 200 pixel area against increasing integration times. The residual plot is the deviation from the linear regression as a percentage.

sense node capacitance at increasing charge levels. Previous work has modeled and corrected for this using a quadratic function [31]. A quadratic in the form $\text{ADU}(t) = a_1 t + a_2 t^2$ is fit to the data, with the inverse function used to convert the ADU into the time domain (proportional to illuminance), given by (6).

The signal versus time (m_1) where the system gain is measured (1112.5 ADU) is then multiplied for gain conversion in e^-/ADU. After the correction is applied, nonlinearity fell to 0.7%. When correcting in the stacked region, the signal ADU is first divided by the FWC increase, N, before linearity correction

$$t(\text{ADU}) = \frac{-a_1 + \sqrt{a_1^2 - 4\ a_2 \text{ADU}}}{2a_2} \quad \{\text{ADU}\ \epsilon\ R \mid 0 \leq \text{ADU} \leq \text{LFWC}\}. \tag{6}$$

4) Dark Current: The dark current of CIS115 is calculated at room temperature by taking nine integrations with the integration time varying from 0 to 4000 ms. This does not include the read time of 10 ms for the 200 $\times$ 200 window. Dark current is found for every pixel in the stack and plot as a distribution in Fig. 5. Mean dark current was found to be 17.0 e^-/pix/s with a dark signal nonuniformity of 12.3 e^-/pix/s. The distribution has a tail of pixels with high dark current. As mentioned previously, dark current is dependent on temperature in an exponential fashion, so changes in device temperature could erroneously impact the results. All data are reduced with dark frames of equivalent length to help mitigate this.

Fig. 6 shows the dark frame noise distributions for the standard and HDR schemes during the imaging session in which data for Section IV were obtained. For the standard scheme, dark current contributions, $\sqrt{I_{\text{dc}} t}$, dominate over read noise, whereas in the HDR scheme, the N reads result in read noise increasing by a factor of $\sqrt{51}$. By using a simple noise model consisting of read and dark current noises [see (7)], where σ_n is the total noise and t the integration time, the

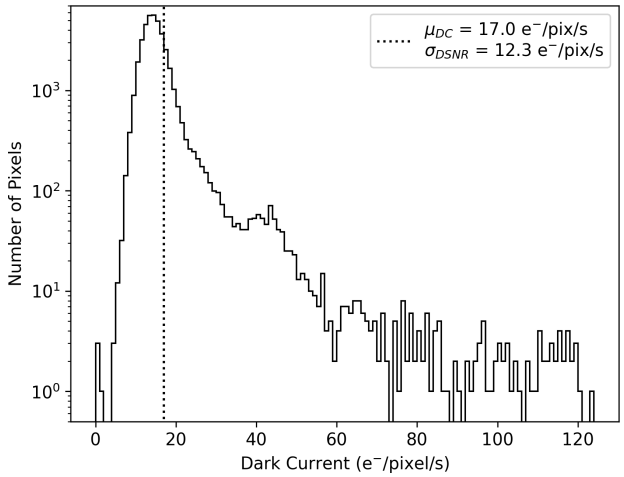

Fig. 5. Dark current distribution for 200 × 200 pixels, bin width of 1 e⁻/pixel/s. Dotted line represents the average dark current. The distribution has a component that follows the normal distribution, as well as a tail of pixels with high dark current. Measurements were taken at 294 K.

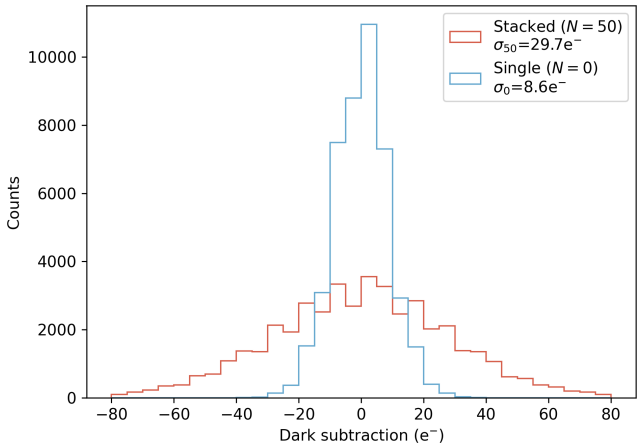

Fig. 6. Noise distribution of dark frames for rows in the HDR scheme (red) and standard scheme (blue), bin width of 5 e⁻. Noise increases from 8.6 to 29.7 e⁻ in the $N = 50$ regions due to the read noise adding in quadrature.

dark current is 35.4 e⁻/pix/s, greater than the value found previously at 17.0 e⁻/pix/s. This is due to heating effects, as the PCB and sensor warm up with continual measurements and the sensitive response of dark current to temperature

$$\sigma_n = \sqrt{(N+1) \times \sigma_{\text{read}}^2 + I_{\text{dc}} t}. \tag{7}$$

5) Line Profile: The HDR and standard readout schemes are compared using a fixed optics setup to project the Airy disk described previously. T_{total} is 1660 ms for both with N of 50 readouts in the HDR scheme. Row wide line profiles are taken for the first and third Airy reflections allowing comparisons of the schemes in high and low signal regions. Dark frames of equivalent length are subtracted then artifacts corrected for. Centroids of the Airy disks are first located using a 2-D Gaussian fitter and window of size 100 pixels. To the nearest pixel, the first reflection is located at (1512, 951) and third at (315, 933). A measurement error is taken as the square root of the signal per pixel as from Poisson statistics.

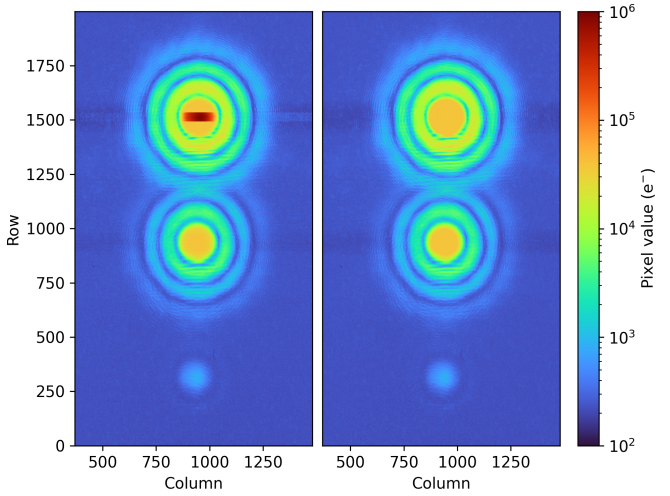

Fig. 7. Comparison of the three reflected Airy patterns using the HDR and standard readout schemes. Left: Airy pattern using the HDR scheme. Right: same pattern with the standard scheme. The majority of pixels in the first-order ring of the primary and secondary reflections are saturated at 25 ke⁻. By contrast, pixels up to 937 ke⁻ are recorded in the linear regime for the HDR region.

Airy and Gaussian profiles are fit in a window from columns 700 to 1200 as this is where the spatial filter was placed to null Airy rings beyond the second (see Fig. 7). Fit parameters for the Airy disk are intensity, width ($ka\mu/h$, converted to FWHM), and centroid location. For the Gaussian of the fainter third profile, these are intensity, width (σ), centroid location, and offset. All are calculated by weighted least squares using the Levenberg–Marquardt algorithm

$$\int_{-4}^{4} \frac{1}{8} \left(\frac{J_1(r_p ka\mu/h)}{r_p ka\mu/h} \right)^2 dr_p = 0.998. \tag{8}$$

Quantitative noise measurement in Fig. 10 uses a nine-row three-column window for noise estimation after light frame subtraction. Due to the nonuniform illumination, shot noise has a spatial variation that increases with window size. The worse case scenario for this is at $r_p = 0$, due to the average photosignal being 0.2% lower than I_0 [see (8)]. At I_0 of 1.0 Me⁻, this corresponds to 2.0 ke⁻. The average deviation in this region is 630 e⁻. As the shot noise in this region 1 ke⁻, this effect is in the subelectron level and so is ignored. The window of 27 pixels is chosen to give enough points for a robust noise estimation while minimizing the aforementioned effect.

IV. Results

A. High Signal Analysis

Maximum photosignal using the HDR scheme in the stacked region, shown by rows containing red pixels in Fig. 7, was measured to be 937 ke⁻ compared to 40 ke⁻ for a single read. This means that parts of the projected Airy disk saturated during standard readout but were entirely within the linear regime of the HDR readout scheme. Horizontal line profiles through the centroid of the first reflection are shown in Fig. 8. A least-squares fit of an Airy disk to the data gives an FWHM of 83.1 ± 0.2 pix and I_0 of 881 ± 4 ke⁻. Average background

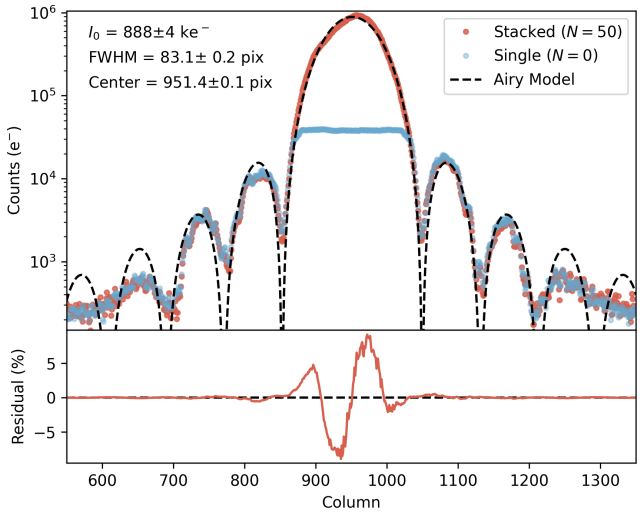

Fig. 8. Reduced line profiles of first Airy reflection using HDR and standard readout modes. HDR data are fit to an Airy to model allowing for parameter extraction. The standard scheme clips at pixel saturation. Residuals of HDR line profile deviate beyond error bars imposed by Poisson statistics, signifying that deviations in fit are from optical interference and misalignment.

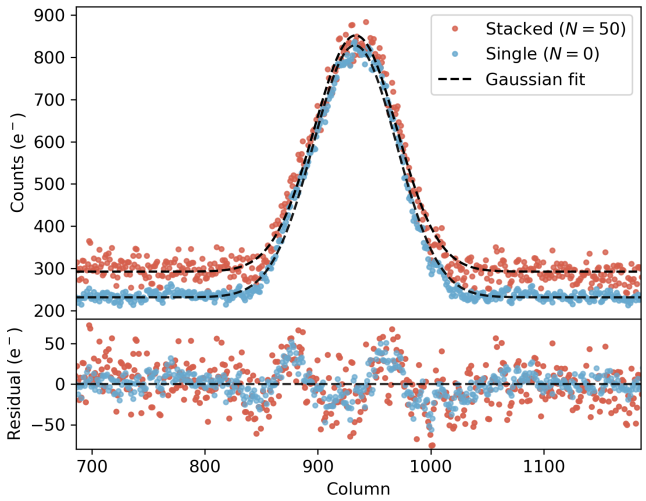

Fig. 9. Reduced line profiles of third Airy reflection using HDR and standard readout modes. The HDR scheme shows both higher background noise (34 versus 15 e$^-$) and background offset (295 versus 234 e$^-$) compared to the standard readout. Both models are fit to a Gaussian as opposed to an Airy disk as the noise washes out all but the first order.

signal and standard deviation are measured using columns 0–500 of the line profiles to avoid sampling the Airy disk. Values are 236 ± 44 e$^-$ for the HDR and 220 ± 15 e$^-$ for the standard scheme. The HDR profile fits the model better than the standard readout as it remains within the linear region of 1015 ke$^-$, whereas the standard readout saturates and clips the data. Higher spatial frequency deviations from the fit of 80 ke$^-$ are present, shown by the sinusoidal in the residuals. These can be explained entirely by the optics, namely, interference from the spatial filter, coherence length differences through the plate, optical imperfections, optical alignment, and scattered light. The Airy function has repeating minima, and light scattering is explained by the photosignal being above 1 ke$^-$ at the first minima. This is difficult to mitigate against when the source irradiance is three orders of magnitude greater.

B. Low Signal Analysis

The impact of an increased noise floor when measuring small photosignals is demonstrated by taking the line profiles as above for the faintest third Airy disk shown in Fig. 9. A Gaussian fit with background offset model is employed as orders beyond the first are swamped by the background noise. Fit parameters using weighted least squared for the profiles in the range 700–1200 columns are given in Table II. The standard scheme has a lower noise floor of 15 e$^-$ compared to the HDR scheme at 34 e$^-$, visible in the residuals of Fig. 9. The background signal of the HDR scheme is 292 e$^-$, significantly greater than the standard scheme at 231 e$^-$ and both background values in the high signal region. This could be due to the previously mentioned signal-dependent baseline shift. As a result of the lower noise in the standard scheme, centroiding of the Gaussian FWHM is improved for the standard readout compared to HDR with respective 1σ uncertainties of 0.2 and 0.3 pixels. Uncertainties in all other model parameters are lower for the standard scheme (see Table II).

TABLE II
GAUSSIAN FIT PARAMETERS FOR FIG. 9

	Single readout	Stacked readout
I_0 (e$^-$)	597±3	560±4
σ (e$^-$)	36.9±0.2	36.5±0.3
Centre (pix)	932.9±0.2	933.4±0.3
Offset (e$^-$)	231±1	292±2

C. SNR Analysis

Fig. 10 shows the distribution of noise against signal for the HDR (red) and standard (blue) schemes, as shown in Fig. 8. Simulated noise performance is overlaid as calculated in Fig. 2 by noise $= ((N+1) \times 4.1^2 + S)^{1/2}$ (e$^-$), where S is the signal in e$^-$. For both schemes, the measured noise bisects the simulated noise until the LFWC is reached. Noise is significantly higher in the stacked scheme at low signals until approximately 3 ke$^-$ where shot noise makes up 90% of the total noise (see Fig. 2). This could be taken as the selection criteria for where to position rows read once. Signals beyond the LFWC of the standard scheme create an island of data points that deviate significantly below the expected signal shot noise due to sensor saturation. The HDR scheme extends beyond this with data bisecting the simulated noise to the LFWC of 984 ke$^-$, validating the linearity preserving behavior of this method.

D. DR Analysis

For a given imaging target, HDR readout rows can be interlaced with a standard readout, with the benefit of lower baseline noise in low signal regions (Fig. 9) and arbitrarily high FWC in high signal regions (Fig. 8). For calculations of DR, the read noise is used as the noise floor. This is because

TABLE III
COMPARATIVE SUMMARY OF HDR EXTENSION DEMONSTRATIONS

	This paper	[21]	[8]	[13]	[18]
Method	Row-wise coded exposure	Block coded exposure	Self reset	Non-destructive readout	Row alternating exposure
Pitch (μm)	7.0	5.0	20.0	16.0	10.0
Array size	2000×1504	512×800	16×16	2048×2048	2800×1088
Read noise (e^-)	4.1	-	-	9.8 (1 NDR)	2.6
Linear FWC (e^-)	19,680	-	-	20,000	100,000
DR (dB)	107.6 (50 samples)	120	121	144 (200 NDR)	120
Relative fill factor	High	High	Low	High	High
DR fidelity	Per row	Per 32×32 block	Per pixel	Per pixel	Per alternating row
PSNR increase	Yes	No	Yes	No	Limited (from dual gain)

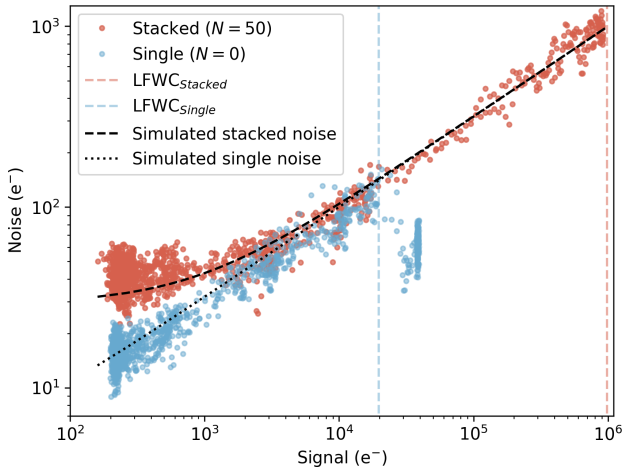

Fig. 10. First reflection line profile noise (estimated with 9 × 3 window) versus window mean for HDR, standard scheme, and expected shot noise. The HDR scheme is in a read noise dominated regime at low signals (<3 ke^-), whereas the standard scheme remains in a shot noise regime. Noise for the HDR scheme follows Poisson statistics until peak intensity at 984 ke^-, whereas the standard readout hits saturation.

of experimental limitations, as dark current noise and stray light shot noise were dominant. Active cooling and the use of a flat illumination source have been used to suppress both sources in similar CIS devices [32].

Compared to the standard readout scheme, interleaving readouts in high signal regions results in an increase in DR from 73.6 to 107.6 dB. Minimum exposure time is increased, depending on the number of additional row reads. Critically, the extended DR stays in the linear regime of the CIS, with the ability to correct for nonlinearity. In this work, readout order was predefined for a known scene, and however, a shortened subexposure and readout order optimization algorithm could dynamically adapt the row readout order to maximize the DR.

E. Applications

A future implementation of this technique is for actively stabilized astronomical spectroscopy, where it is desirable for both calibration spectral lines and science (observation performed) spectral lines to have the same optical path to the focal plane. Stability is achieved through the continuous generation of corrections to the focal plane from the centroids of calibration spectral lines [24]. These continuous small corrections are possible because the brighter calibration signal is read out frequently, while the fainter stellar science signal builds up on adjacent regions of the detector, which are read out at a much lower rate. Emission lines from traditional calibration sources can also vary in strength. Maximizing uniformity in intensity and, therefore, effective spatial uniformity in all regions of interest leads to the potential for more precise corrections to the focal plane [25]. This in turn enables more precise scientific measurements. Although the laser-comb technology has resolved these nonuniformity issues, they are much more expensive to build and maintain and do not overcome the issue of focal plane stability.

In principle, there are also a variety of other applications where multicadence ROIs might be important. As with the case of astronomical spectroscopy, telescope time on the target is a very valuable commodity. In most types of astronomical imaging, it is desirable to obtain the longest exposure and highest DR possible before taking the penalty of readout noise. For example, when trying to discriminate planets in orbit around stars there is typically a contrast ratio in excess of a million, and thus, there are many different techniques used to reduce the contrast ratio [26] and make signal detection more manageable for detectors.

V. CONCLUSION

An implementation of row-wise coded exposure using a CIS115 increased the DR from 73.6 to 107.6 dB and PSNR from 42.9 to 59.9 dB. The utility of this operation is demonstrated whereby the linear FWC in high signal "calibration" regions was extended 50 times with an interlaced readout order, while the noise floor remained unchanged with a single readout in low signal "science" regions. The DR can be extended arbitrarily high by reading out a row multiple times. This scheme resulted in an increase of centroiding precision in low signal regions due to the single read while extending the linear FWC via multiple readouts. Row readout order needs to be predefined making it more suitable for well-known scenes with little temporal variation. Further work would involve a working demonstration in an echelle spectrograph and the exploration of simultaneous ROI imaging at varying subexposure durations.

A comparative summary is given in Table III. Although this article achieves the smallest absolute DR compared to other works in this table, the extension range is not hardware-based and thus can be increased to a user-defined level at the cost of increased minimum integration time. By increasing the number

of reset and read samples from 50 to 200, the DR extension demonstrated in this article would increase to 120 dB. This is achieved on the 7.0-μm pitch while preserving linearity. The only other technique to extend PSNR continuously is the self-reset pixel, which comes at the cost of low fill factor. In this work, the DR is increased on a per row basis; independent column addressability would extend the method to DR increase per pixel [16].

ACKNOWLEDGMENT

The authors acknowledge the support of Teledyne e2v for providing CIS115. They also thank Andrew Pike, Douglas Jordan, and Paul Jerram from Teledyne e2v for their support.

Data underlying the results presented in this paper can be requested by emailing t.wocial@herts.ac.uk.

REFERENCES

[1] J. Pratlong, S.-Y. Wang, M. Lehner, P. Jorden, P. Jerram, and S. Johnson, "A 9 megapixel large-area back-thinned CMOS sensor with high sensitivity and high frame-rate for the TAOS II program," *Proc. SPIE*, vol. 9915, Jul. 2016, Art. no. 991514, doi: 10.1117/12.2233034.

[2] E. R. Fossum, "CMOS image sensors: Electronic camera-on-a-chip," *IEEE Trans. Electron Devices*, vol. 44, no. 10, pp. 1689–1698, Oct. 1997, doi: 10.1109/16.628824.

[3] D. X. D. Yang and A. El Gamal, "Comparative analysis of SNR for image sensors with enhanced dynamic range," *Proc. SPIE*, vol. 3649, pp. 197–211, Apr. 1999, doi: 10.1117/12.347075.

[4] A. Spivak, A. Belenky, A. Fish, and O. Yadid-Pecht, "Wide-dynamic-range CMOS image sensors—Comparative performance analysis," *IEEE Trans. Electron Devices*, vol. 56, no. 11, pp. 2446–2461, Nov. 2009, doi: 10.1109/TED.2009.2030599.

[5] B. Fowler et al., "A 5.5Mpixel 100 frames/sec wide dynamic range low noise CMOS image sensor for scientific applications," *Proc. SPIE*, vol. 7536, Feb. 2010, Art. no. 753607, doi: 10.1117/12.846975.

[6] Z. Li, X. Wang, B. Li, and Y. Chang, "160 dB dynamic range pixel with charge compensation for CMOS image sensor," *Electron. Lett.*, vol. 52, no. 10, pp. 819–821, May 2016, doi: 10.1049/EL.2015.4484.

[7] J. A. Leñero-Bardallo, R. Carmona-Galán, and A. Rodríguez-Vázquez, "A wide linear dynamic range image sensor based on asynchronous self-reset and tagging of saturation events," *IEEE J. Solid-State Circuits*, vol. 52, no. 6, pp. 1605–1617, Apr. 2017, doi: 10.1109/JSSC.2017.2679058.

[8] S. Hirsch, M. Strobel, W. Klingler, J. D. S. Spüntrup, Z. Yu, and J. N. Burghartz, "Realization and opto-electronic characterization of linear self-reset pixel cells for a high dynamic CMOS image sensor," *Adv. Radio Sci.*, vol. 17, pp. 239–247, Sep. 2019, doi: 10.5194/ARS-17-239-2019.

[9] S. Mann, "Compositing multiple pictures of the same scene," in *Proc. IS&T Annu. Meeting*, 1993, pp. 50–52.

[10] O. Yadid-Pecht and E. R. Fossum, "Wide intrascene dynamic range CMOS APS using dual sampling," *IEEE Trans. Electron Devices*, vol. 44, no. 10, pp. 1721–1723, Oct. 1997, doi: 10.1109/16.628828.

[11] M. Sasaki, M. Mase, S. Kawahito, and Y. Tadokoro, "A wide-dynamic-range CMOS image sensor based on multiple short exposure-time readout with multiple-resolution column-parallel ADC," *IEEE Sensors J.*, vol. 7, no. 1, pp. 151–158, Jan. 2007, doi: 10.1109/JSEN.2006.888058.

[12] A. Kachatkou and R. van Silfhout, "Dynamic range enhancement algorithms for CMOS sensors with non-destructive readout," in *Proc. IEEE Int. Workshop Imag. Syst. Techn.*, Sep. 2008, pp. 132–137, doi: 10.1109/IST.2008.4659956.

[13] G. R. Sims et al., "A CMOS visible image sensor with non-destructive readout capability," *Proc. SPIE*, vol. 10709, Jul. 2018, Art. no. 107090V, doi: 10.1117/12.2314144.

[14] J. D. Offenberg et al., "Validation of up-the-ramp sampling with cosmic-ray rejection on infrared detectors," *Publications Astronomical Soc. Pacific*, vol. 113, no. 780, p. 240, Feb. 2001, doi: 10.1086/318615.

[15] J. Gu, Y. Hitomi, T. Mitsunaga, and S. Nayar, "Coded rolling shutter photography: Flexible space-time sampling," in *Proc. IEEE Int. Conf. Comput. Photography (ICCP)*, Mar. 2010, pp. 1–8, doi: 10.1109/ICCPHOT.2010.5585094.

[16] D. Liu, J. Gu, Y. Hitomi, M. Gupta, T. Mitsunaga, and S. K. Nayar, "Efficient space-time sampling with pixel-wise coded exposure for high-speed imaging," *IEEE Trans. Pattern Anal. Mach. Intell.*, vol. 36, no. 2, pp. 248–260, Feb. 2014, doi: 10.1109/TPAMI.2013.129.

[17] H. Cho, S. J. Kim, and S. Lee, "Single-shot high dynamic range imaging using coded electronic shutter," *Comput. Graph. Forum*, vol. 33, no. 7, pp. 329–338, 2014, doi: 10.1111/cgf.12501.

[18] B. Dupont et al., "A dual-core highly programmable 120dB image sensor," *Electron. Imag.*, vol. 28, no. 12, pp. 1–3, Feb. 2016, doi: 10.2352/ISSN.2470-1173.2016.12.IMSE-261.

[19] Y. Oike, "Evolution of image sensor architectures with stacked device technologies," *IEEE Trans. Electron Devices*, vol. 69, no. 6, pp. 2757–2765, Jun. 2022, doi: 10.1109/TED.2021.3097983.

[20] T. Hirata, H. Murata, H. Matsuda, Y. Tezuka, and S. Tsunai, "7.8 A 1-inch 17Mpixel 1000fps block-controlled coded-exposure back-illuminated stacked CMOS image sensor for computational imaging and adaptive dynamic range control," in *IEEE Int. Solid-State Circuits Conf. (ISSCC) Dig. Tech. Papers*, Feb. 2021, pp. 120–122, doi: 10.1109/ISSCC42613.2021.9365740.

[21] A. Peizerat et al., "A 120dB DR and 5μm pixel pitch imager based on local integration time adaptation," in *Proc. Int. Image Sensor Workshop*, 2015, pp. 385–388.

[22] R. Ikeno et al., "A 4.6-μm, 127-dB dynamic range, ultra-low power stacked digital pixel sensor with overlapped triple quantization," *IEEE Trans. Electron Devices*, vol. 69, no. 6, pp. 2943–2950, Jun. 2022, doi: 10.1109/TED.2021.3121352.

[23] Teledyne. (2017). *CIS115 Back-Side Illuminated CMOS Image Sensor*. Accessed: Feb. 14, 2022. https://www.teledyne-e2v.com/shared/content/resources/A1A-785580-Ver3-CIS115Datasheet.pdf

[24] H. R. A. Jones et al., "A small actively controlled high-resolution spectrograph based on off-the-shelf components," *PASP*, vol. 133, no. 1020, p. 025001, Jan. 2021, doi: 10.1088/1538-3873/abc7ee.

[25] C.-H. Li et al., "A laser frequency comb that enables radial velocity measurements with a precision of 1 cm s^{-1}," *Nature*, vol. 452, no. 7187, pp. 610–612, Apr. 2008, doi: 10.1038/nature06854.

[26] W. A. Traub and B. R. Oppenheimer. (2010). *Direct Imaging of Exoplanets*. 2010. Accessed: May 11, 2022. [Online]. Available: https://ui.adsabs.harvard.edu/abs/2010exop.book.111T

[27] M. Knapp et al., "Demonstrating high-precision photometry with a CubeSat: ASTERIA observations of 55 Cancri e," *Astronomical J.*, vol. 160, no. 1, p. 23, Jun. 2020, doi: 10.3847/1538-3881/ab8bcc.

[28] T. Greffe et al., "Characterization of low light performance of a complementary metal-oxide semiconductor sensor for ultraviolet astronomical applications," *J. Astronomical Telescopes, Instrum., Syst.*, vol. 8, no. 2, Apr. 2022, Art. no. 026004, doi: 10.1117/1.jatis.8.2.026004.

[29] D. A. Starkey and E. R. Fossum, "Determining conversion gain and read noise using a photon-counting histogram method for deep sub-electron read noise image sensors," *IEEE J. Electron Devices Soc.*, vol. 4, no. 3, pp. 129–135, May 2016, doi: 10.1109/JEDS.2016.2536719.

[30] M. Soman et al., "Design and characterisation of the new CIS115 sensor for JANUS, the high resolution camera on JUICE," *Proc. SPIE*, vol. 9154, Jul. 2014, Art. no. 915407, doi: 10.1117/12.2056810.

[31] M. Soman, K. Stefanov, D. Weatherill, A. Holland, J. Gow, and M. Leese, "Non-linear responsivity characterisation of a CMOS active pixel sensor for high resolution imaging of the Jovian system," *J. Instrum.*, vol. 10, no. 2, Feb. 2015, Art. no. C02012, doi: 10.1088/1748-0221/10/02/c02012.

[32] S.-Y. Wang et al., "The characteristic of teledyne e2v CIS 113 CMOS sensors," *Proc. SPIE*, vol. 11454, Dec. 2020, Art. no. 114542P, doi: 10.1117/12.2561204.